Article:
Mullis, AM (2014) A phase-field model for the diffusive melting of isolated dendritic fragments. Metallurgical and Materials Transactions A: Physical Metallurgy and Materials Science, 45 (7). 3097 - 3102. ISSN: 1073-5623

https://doi.org/10.1007/s11661-014-2252-y

A Phase-Field Model for the Diffusive Melting of Isolated Dendritic Fragments

Andrew M. Mullis

Institute for Materials Research, University of Leeds, Leeds LS2-9JT, UK.

Abstract

A thermal phase-field model constructed in the 'thin-interface' limit and incorporating a number of advanced numerical techniques as such adaptive mesh refinement, implicit time-stepping and a multigrid solver has been used to study the isolated diffusive melting of dendritic fragments. The results of the simulations are found to be fully consistent with the experimental observation of such melting in microgravity during the Isothermal Dendrite Growth Experiment. It is found that the rate at which the ratio of semi-major to semi-minor axes changes is a function of the melt Stefan number, which may help explain why both melting at (approximately) constant ratio and melting at slowly increasing ratio have been observed.

1. Introduction

Following the recent publication of a series of papers [1, 2, 3] relating to the cyclic melting of material as part of the Isothermal Dendrite Growth Experiment (IDGE) there has been a resurgence of interest in the melting of dendritic crystal fragments. Three IDGE experiments were flown [4, 5, 6] in the cargo bay of the space shuttle in order to study the dendritic solidification of the plastic crystals succinonitrile (SCN) and pivalic anhydride (PVA) in the very stable, low gravity environment provided by this platform. Therefore, unlike terrestrial melting experiments in which the fragments experience sedimentation due to the density difference between the solid and liquid phases, the dendritic fragments observed during the melting phase of the IDGE remained stationary within their parent melt. The consequent elimination of Stoke's flow means that the heat transfer between the crystal and the melt can, to a very high degree of precision, be regarded as purely diffusive.

During the IDGE experiments the SCN (IDGE-1 & 2) or PVA (IDGE-3) test substances were brought to a uniform undercooling at which they were held to within $\pm$ 0.002 K prior to the nucleation of crystallisation. Following nucleation an array of dendritic crystals would propagate into the melt, the growth of which could be observed and photographically recorded through the transparent SCN or PVA melt. The results thus obtained have provided an invaluable data set against which theories of dendritic growth have been tested, including verification of the Ivantsov relationship [7] between undercooling and growth Peclet number [8] and that the radius selection eigenvalue, σ^*, is not constant but varies with undercooling [9]. Once the growth phase was complete the temperature was raised in order to remelt the dendritic mush so that the cycle could be repeated. As the focus of the experiment was the solidification stage of the process, not the subsequent remelting, the remelting phase was much less carefully controlled and less well recorded. Despite this, during

the final IDGE experiment video data of around 100 melting cycles in PVA was captured at 30 fps. It is the analysis [1, 2, 3] of these data that has stimulated the renewed interest in the melting of dendritic fragments.

The quantitative analysis of the melting of dendritic fragments conducted by [1, 2, 3] was generally restricted to the later stages of the melting cycle, wherein the complex interpenetrating array of side-branches can be reduced to a series of isolated crystals. Moreover, the almost complete melting back of secondary and tertiary arms gives rise to fragments, each of which can be approximated closely as a figure of revolution with an elliptic cross-section. These ellipsoidal crystallites were characterised by their semi-major and semi-minor axes, $\mathscr{C}$ and $\mathscr{A}$, respectively. The primary conclusions of this analysis were that for the majority of the melting phase the ratio $\mathscr{C}/\mathscr{A}$ would either remain approximately constant [1] or would increase slowly with time [2] but that in the very final stages of melting $\mathscr{C}/\mathscr{A}$ would collapse rapidly toward 1, such that at extinction the fragments were always spherical. This phenomenon was attributed to capillarity effects whereby the higher curvature, and consequentially slightly depressed melting temperature, at the tip of the elliptic fragment relative to its equator gave rise to a heat flow from the equator towards the tip which would accelerate melting near the tip, thereby reducing the $\mathscr{C}/\mathscr{A}$ ratio towards unity [1, 2]. However, due to the small length scales associated with capillary effects, this equalisation of $\mathscr{C}$ and $\mathscr{A}$ would naturally be restricted to the terminal stages of melting, as observed experimentally.

Simulation of the melting phenomenon was undertaken [1, 3] using a quasi-static model in which the dendritic fragment was assumed to be an ellipsoid of revolution with fixed $\mathscr{C}/\mathscr{A}$ ratio. The Gibbs-Thomson relationship was used to establish the surface temperature of the ellipsoidal dendrite fragment and the conduction equation solved to calculate the heat flow into the crystal from the surrounding liquid. The volume rate of melting was then calculated and the size of the crystal reduced accordingly, whilst maintaining $\mathscr{C}/\mathscr{A}$ as a constant. This model appears to give excellent agreement with regard to the rate at which $\mathscr{C}$ decreases with time but, by virtue of the assumed constant $\mathscr{C}/\mathscr{A}$ ratio, is unable to demonstrate the capillary mediated spheroidisation of the crystal during the terminal stages of melting.

In this paper we use a thermal phase-field model to solve for the evolution of an initially elliptic dendrite fragment as it melts in its superheated parent melt. In contrast to the quasi-static model used in [1, 3] the phase-field model solves the free boundary problem so we neither have to assume a constant $\mathscr{C}/\mathscr{A}$ nor indeed that the fragment retains an elliptic section during melting. Consequently, we can independently test, using a well established simulation methodology, whether or not capillary forces drive melting fragments towards an aspect ratio of unity as they approach extinction. The downside to the phase-field methodology is its highly computationally intensive nature. For this reason we have restricted the simulations presented here to 2-dimensions.

2. Description of the Model

We use a standard phase-field model based upon that presented by Karma & Rappel [10, 11]. Following non-dimensionalization against characteristic length and time

scales, W_0 and τ_0, the evolution of the phase-field, ϕ, when expanded [12] into the form used in the numerical implementation presented below, is given by

$$A^2(\psi)\frac{\partial\phi}{\partial t} = \nabla\cdot\left(A^2(\psi)\nabla\phi\right) + \phi(1-\phi^2) - \lambda\theta(1-\phi^2)^2$$
$$-\frac{\partial}{\partial x}\left(A(\psi)A'(\psi)\frac{\partial\phi}{\partial y}\right) + \frac{\partial}{\partial y}\left(A(\psi)A'(\psi)\frac{\partial\phi}{\partial x}\right) \quad (1)$$

where the solid and liquid phases correspond to $\phi = 1$ and $\phi = -1$ respectively, $\psi = \arctan(\phi_x/\phi_y)$ is the angle between the normal to the interface and the x-axis and $A(\psi) = 1 + \varepsilon.\cos(\eta\psi)$ is an anisotropy function with strength ε and mode number η. The dimensionless coupling parameter, λ, is given by [10] as

$$\lambda = \frac{D}{a_2} = \frac{a_1 W_0}{d_0} \quad (2)$$

where D is the thermal diffusivity and in order to simulate kinetic free growth it is shown in [11] that a_1 and a_2 take the values $5\sqrt{2}/8$ and 0.6267 respectively. The capillary length scale, d_0, is given by

$$d_0 = \frac{T_m c_p \gamma}{\rho L^2} \quad (3)$$

with T_m being the melting temperature, L the latent heat of fusion, c_p the specific heat capacity, ρ the density and γ the interfacial energy between the solid and liquid.

The evolution of the dimensionless temperature field, θ, is given by

$$\frac{\partial\theta}{\partial t} = D\nabla^2\theta + \frac{1}{2}\frac{\partial\phi}{\partial t} \quad (4)$$

where θ is related to physical temperature, T, via

$$\theta = \frac{T - T_m}{L/c_p} \quad (5)$$

The governing equations are descretized using a finite difference approximation based upon a quadrilateral, non-uniform, locally-refined mesh with equal grid spacing in both directions [13, 14]. This allows the application of standard second order central difference stencils for the calculation of first and second differentials, while a compact 9-point scheme has been used for Laplacian terms, in order to reduce the mesh induced [15] anisotropy. To ensure sufficient mesh resolution around the interface region and to handle the multi-scale nature of the problem local mesh refinement (coarsening) is employed when the weighted sum of the gradients of ϕ and θ exceeds (falls below) some predefined value.

A potential draw back of using adaptive mesh refinement when using an explicit solution scheme is that the time step scales as h^2, where h is the mesh spacing at the finest refinement level. On heavily refined meshes this can lead to unfeasibly small time steps. In order to overcome this limitation an implicit temporal descretization is employed here based on the second order Backward Difference Formula with variable time-step. This is an A-stable [16] implicit linear 2-step method for which we have previously demonstrated that the time-step is independent of h.

When using implicit time discretisation methods it is necessary to solve a very large, but sparse, system of non-linear algebraic equations at each time-step. Multigrid methods are among the fastest available solvers for such systems and in this work we apply the non-linear generalization known as FAS (full approximation scheme [17]). The local adaptivity is accommodated via the multilevel algorithm originally proposed by Brandt [18]. The interpolation operator is bilinear while injection is used for the restriction operator. For smoothing the error we use a fully-coupled nonlinear weighted Gauss-Seidel iteration where the number of pre- and post-smoothing operations required for optimal convergence is determined empirically. Full details of the numerical scheme are given in [13, 14].

3. Results and Discussion

Phase-field simulations of melting have been undertaken by starting from an initial solid seed with an elliptical section. The geometry of the seed is therefore uniquely defined by its semi-major and semi-minor axes, $\mathscr{E}$ and $\mathscr{A}$, respectively. The normalised temperature of the seed is taken as $\theta = 0$ (equivalent to setting $T = T_m$ in the solid). Due to curvature effects this will be marginally above the local equilibrium melting temperature, although this small effective superheating of the initial solid results in negligible melting. The surrounding liquid, and the far field boundary of the domain, are set to a uniform normalised temperature of $\theta = \mathrm{St}^+$, where St^+ is the melting Stefan number. This equivalent in our non-dimensional scheme to defining

$$\mathrm{St}^+ = \frac{T_\infty - T_m}{L / c_p} \tag{6}$$

where T_∞ is the far-field temperature. This is the identical definition to that used in [2, 3]. The computational domain, Ω, is taken to be very large, relative to the semi-major axis, $\mathscr{E}$, of the fragment. Here we take very large to mean that if we apply a Dirichlet condition on the domain boundary, such that its temperature is fixed at St^+, the thermal gradient at all points on the boundary remains 0 throughout the solution. In this way the boundary does not influence the melting behaviour of the dendritic fragment and the solution is rendered independent of the actual size of the domain. From a practical point of view we find that using a domain of $\approx 15\,\mathscr{E}$ is large enough for this condition to be maintained. Fortunately, the adaptive nature of the numerical scheme means that very few elements are required far from the melting fragment and consequently the computational overhead on using such a large domain is minimal.

Simulations have been undertaken for Stefan numbers in the range 0.1 – 0.4, which gives some overlap with experiment, where the maximum Stefan number applied to PVA during the IDGE experiments is 0.16. Most simulations have been conducted at

a melting Stefan number, St^+, of 0.2. This higher Stefan number has been used as the slow melting resulting from the application of a lower Stefan number gives excessive computation time. The effect of the applied Stefan number on the morphology of the melting crystal will be examined later in this section and, as pointed out in [2], was subject to variation from location to location within the experimental apparatus. Also, unless otherwise specified all simulations have been conducted with zero anisotropy. In cases where an anisotropy is imposed this has a four-fold symmetry which is aligned with the semi-major and semi-minor axes.

An example of the change in morphology of an initially elliptic dendrite fragment as it melts is shown in Fig. 1, which gives the contour of $\phi = 0$ (taken here as the location of the solid-liquid interface) at equally spaced time intervals up to the point just prior to extinction. The corresponding value of $\mathscr{E}/\mathscr{A}$ as a function of time, τ, and length of the semi-major axes, $\mathscr{E}$, is given in Fig. 2. In this particular simulation the initial value of $\mathscr{E}$ is $5792d_0$, with $\mathscr{E}/\mathscr{A} = 4$. As can be seen from the Figures the simulations reproduce many of the effects observed experimentally. For the majority of the melting cycle, typically around 75-80% of the total simulation time, the $\mathscr{E}/\mathscr{A}$ ratio increases, albeit very slowly, in this simulation reaching as maximum value of 5.14. Thereafter the $\mathscr{E}/\mathscr{A}$ ratio decreases, return to its initial value of 4 when the crystal is approximately 7% of its original length. During the final stages of its evolution the crystal spheroidises rapidly, with the $\mathscr{E}/\mathscr{A}$ ratio approaching 1 just prior to extinction. As suggested by [1, 2] for the experimental case, we attribute this spheroidisation behaviour to capillary effects, once the crystal becomes sufficiently small for such effects to dominate.

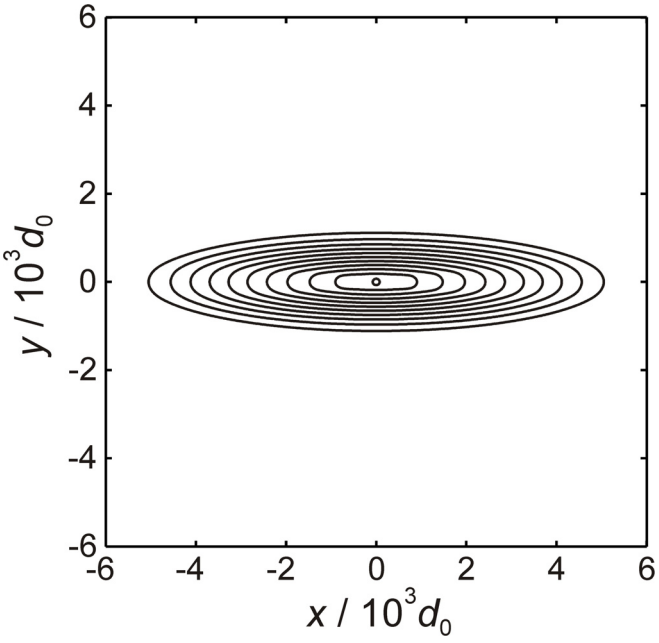

Figure 1. Contour map of the solid-liquid interface showing the evolution of an elliptic dendritic fragment with initial $\mathscr{E} = 5792d_0$ and $\mathscr{E}/\mathscr{A} = 4$. The time interval between contours is constant.

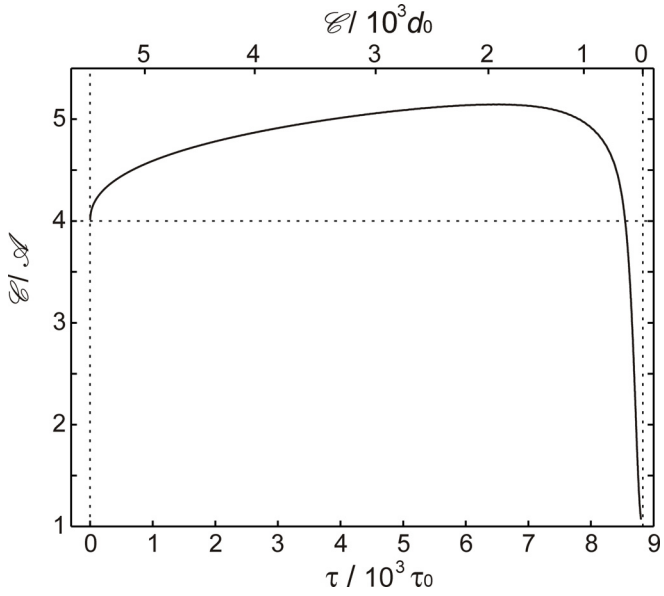

Figure 2. Evolution of the ratio of semi-major to semi-minor axes as a function of time and length of the semi-major axis for an elliptic dendritic fragment with initial $\mathscr{E} = 5792d_0$ and $\mathscr{E}/\mathscr{A} = 4$.

Within the thin interface model the magnitude of capillary effects are determined by the coupling parameter, λ, which determines the size of the characteristic length scale within the model, W_0, relative to the capillary length, d_0. As shown in Equ. (2), this also fixes the diffusivity, D. Consequently, the relative effect of capillarity is uniquely specified by the size of the elliptic seed relative to the capillary length, d_0. This in turn is determined by the size of the seed in terms of W_0 and λ which relates W_0 to d_0. The magnitude of capillary effects can therefore be adjusted by altering $\mathscr{E}/\ W_0$, or λ, or both. In this work values for λ in the range 1 – 32, have been utilised, with values of λ towards the upper end of this spectrum being used to simulate the largest fragments considered and vice versa. By comparison [19] showed that the thin-interface model was still convergent for values for λ of up to 72.1. In the simulation presented in Figures 1 & 2 the semi-major axis of the initial seed is given by $\mathscr{E} = 320W_0$ and $\lambda = 16$, wherein $\mathscr{E} = 5792d_0$.

In order to study the effects of initial crystallite size on the melting behaviour a set of simulations have been conducted, varying $\mathscr{E}$ from $90.5d_0$ to $46340d_0$. As in the previous simulation the initial $\mathscr{E}/\mathscr{A}$ ratio is 4 and the melting Stefan number is 0.2. The results are presented in Fig. 3, in which the evolution of the $\mathscr{E}/\mathscr{A}$ ratio is plotted against the length of the $\mathscr{E}$ axis. However, in order to present the data in a single plot, the semi-major axis $\mathscr{E}$ is plotted on a log scale while for comparability with Fig. 2 we have plotted $\mathscr{E}$ increasing from right to left. For clarity, the data previously presented in Fig. 2 is shown in bold.

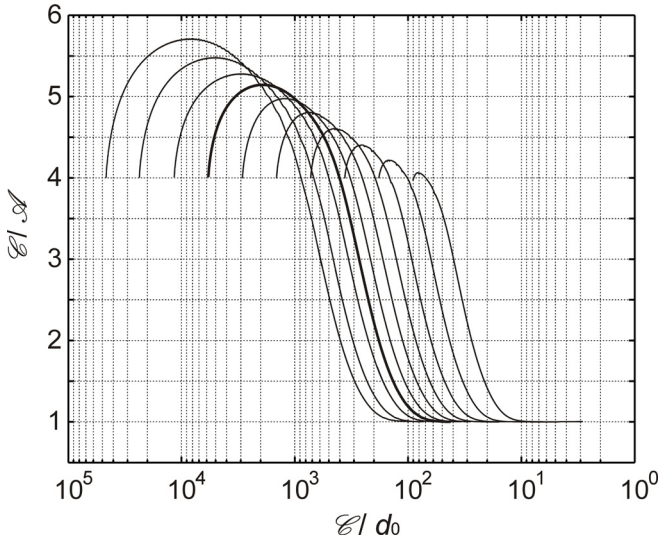

Figure 3. Evolution of the ratio of semi-major to semi-minor axes for dendritic fragments with initial lengths in the range $90.5d_0$ - $46340d_0$. Curve shown bold is for the dendrite depicted in Figures 1 & 2.

We note that the general behaviour of the fragments during melting is independent of their initial size in that, for all cases, the $\mathscr{C}/\mathscr{A}$ ratio initially increases before decreasing again and finally collapsing rapidly to 1. All fragments therefore ended up near spherical just prior to extinction, as observed experimentally by [1, 2]. However, we also note that as the initial fragments become larger, the proportion of the dissolution time during which $\mathscr{C}/\mathscr{A}$ increases also becomes larger. Consequently the maximum value of $\mathscr{C}/\mathscr{A}$ attained increases. Both observations would be consistent with capillarity playing only a very minor role in the initial evolution of large fragments, with capillary effects becoming progressively more important as the size of the fragment decreases. However, it is also clear that it is not possible to identify a single length scale at which capillary effects dominate. Indeed, as the initial size of the fragments increases so does the value of $\mathscr{C}$ at which the maximum in the $\mathscr{C}/\mathscr{A}$ ratio and the point at which $\mathscr{C}/\mathscr{A}$ returns to its initial value. This is probably the result of the, albeit weak, capillary effect having longer to operate due to the increased time to melt the larger fragments.

The effect of the melting Stefan number, St^+, is explored in Figs. 4 and 5, for an initially elliptic fragment with $\mathscr{C}/\mathscr{A} = 4$ and $\mathscr{C} = 11584d_0$, with St^+ being varied from 0.1 to 0.4 in intervals of 0.05. As before, the same general behaviour is observed with all simulations showing first an increase in the $\mathscr{C}/\mathscr{A}$ ratio, followed by a decrease and eventual collapse towards 1 (Fig. 4). However, a significant Stefan number dependence is also apparent. At high Stefan number $\mathscr{C}/\mathscr{A}$ increases more rapidly and peaks at a higher value than at lower Stefan numbers. For $St^+ = 0.4$ the peak value of $\mathscr{C}/\mathscr{A}$ is 7.46, compared with just 4.49 for $St^+ = 0.1$. Moreover, presumably because of the higher values reached by $\mathscr{C}/\mathscr{A}$ during the high Stefan number simulations the value of $\mathscr{C}/\mathscr{A}$ remains above its initial value (in this case 4) for longer. Again, this would be consistent with the spheroidisation of the fragments in the terminal stages of melting being mediated by capillarity, with high Stefan number tending to produce morphologies dominated by heat transfer from the surrounding locale, rather than by capillarity, i.e. $\mathscr{C}/\mathscr{A}$ peaks at a higher value and

the onset of spheroidisation is delayed. The time taken for the complete dissolution of an initial fragment with $\mathscr{C}/\mathscr{A} = 4$ and $\mathscr{C} = 11584d_0$, as a function of the melting Stefan number is shown in Fig. 5. The time for complete melting increases steeply as St^+ decreases, particularly for values below $St^+ = 0.15$, and it is due to the long computation times associated with these low St^+ simulations that the simulations run here have generally been run a somewhat higher Stefan numbers than those that pertain to the experiments reported in [1, 2, 3].

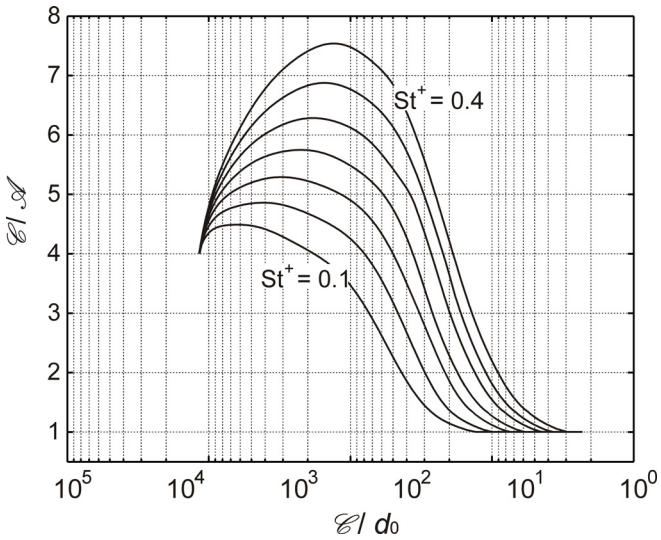

Figure 4. Evolution of the ratio of semi-major to semi-minor axes as a function of Stefan number for elliptic fragments with initial length $11584d_0$. Results shown at 0.05 intervals between $St^+ = 0.1$ and 0.4.

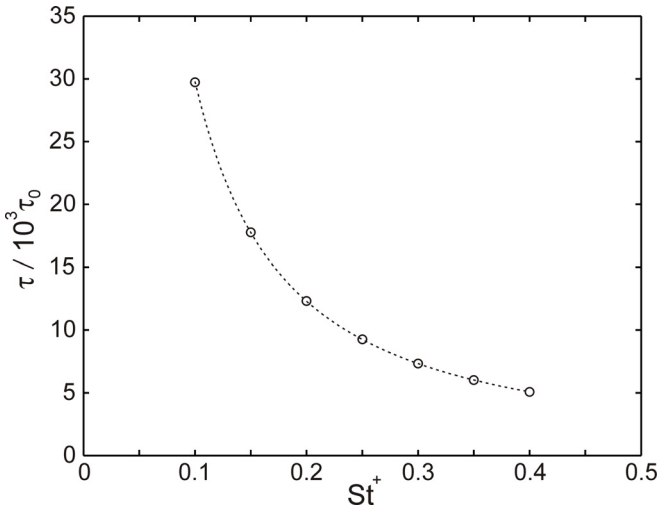

Figure 5. Time taken for the complete melting of a dendritic fragment with initial semi-major axis of $11584d_0$ as a function of melting Stefan number.

The simulations presented above are all calculated on the assumption of an isotropic surface energy, although it is of course the case that a prerequisite to the formation of dendrites is an anisotropic surface energy. However, unlike the case for growth of the solid from the melt, in the case of dissolution of the solid into the melt we find

virtually no dependence upon anisotropy. The effect of surface energy anisotropy has been investigated for $0 \leq \varepsilon \leq 0.05$, and even in the case of the highest surface energy studied ($\varepsilon = 0.05$) we find that the evolution of the dendritic fragment as it melts is essentially identical to that of an equivalent fragment with an isotropic surface energy, with the $\mathscr{C}/\mathscr{A}$ ratio for the anisotropic simulation always being within 0.3% of that for the isotropic simulation at the same point in the evolution. Despite this the presence of anisotropy does alter the morphology of the tip region. This is illustrated in Fig. 6 which shows the region near the tip for two fragments that are identical except that one is growing with an isotropic surface energy and the other with a surface energy anisotropy of 5%. The initial fragment had $\mathscr{C}/\mathscr{A} = 4$ and $\mathscr{C} = 5792d_0$, with the image shown here representing the tip shape after the length had reduced by approximately 20% in order to allow the fragment to adjust to its equilibrium shape, wherein the $\mathscr{C}/\mathscr{A}$ ratio had increased to 4.72. As can be seen from the figure the fragment with an anisotropic surface energy has a considerably higher local curvature at the tip relative to the fragment with the isotropic surface energy. In fact at this point in the evolution the local curvature at the tip for the anisotropic fragment is 2.60 times that for the isotropic fragment, with this ratio remaining approximately constant throughout the majority of the dissolution until spheroidisation of the fragment towards the end of the melting process. In the case of fragments with lower values of anisotropy similar behaviour is observed but with a correspondingly lower ratio between their local curvature and that of the isotropic fragment (1.14, 1.35, 1.62 and 2.02 for anisotropies of 0.01, 0.02, 0.03 and 0.04 respectively). However, despite this difference in the local curvature at the tip there is minimal difference in the rate at which the fragments dissolve and, with the exception of the region close to the tip, the geometry of the fragment is approximated well by an ellipse.

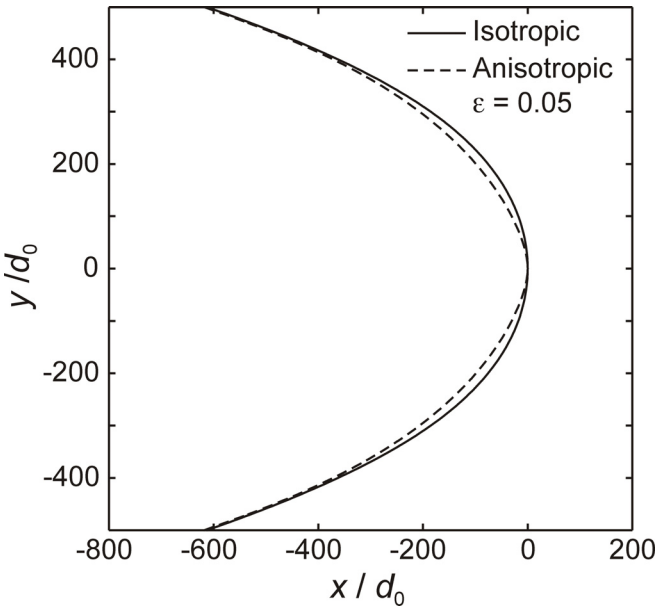

Figure 6. Shape of the tip of the elliptic dendrite fragment in the absence of anisotropy (solid) and with a surface energy anisotropy of 0.05 (dashed). Figure is for a dendrite with initial $\mathscr{C} = 5792d_0$ and $\mathscr{C}/\mathscr{A} = 4$ after melting to ≈ 80% of its starting length.

Overall we find that the results of the phase-field model are consistent both with the experimental data presented by [1, 2, 3] and with the hypothesis that spheroidisation during the terminal stages of melting is mediated by capillary effects lowering the temperature marginally at the fragment tip. Irrespective of the melting conditions we find that fragments are approximated well as being of elliptic cross section and both the overall shape and rate of dissolution are found to be insensitive to the level of anisotropy assumed for the crystal. Moreover, the model may shed light upon one apparent contradiction within the experimental data. In [1] it was reported that the ratio $\mathscr{E}/\mathscr{A}$ would remain approximately constant until the terminal stages of melting whereas in [2] it was found that it would increase slowly with time during the majority of the melting period. We note that from the simulations the melting behaviour has a relatively strong dependence upon the melting Stefan number, with high Stefan numbers causing $\mathscr{E}/\mathscr{A}$ to increase much more rapidly than is the case at low Stefan numbers. We also note that, as pointed out by [3], the average melting Stefan number rises from 0 to a maximum of 0.16 over a period of around 2200 s, during which time melting occurs continuously. Moreover, it is likely that there were spatial, as well as temporal, variations in St^+ [2], with regions where the local Stefan number is reduced due to thermal shielding by the mushy zone [20]. We therefore conjecture that the variation in behaviour occurs due to variations in the local Stefan number, with low values of St^+ corresponding to observations of near constant $\mathscr{E}/\mathscr{A}$ during melting, while higher values of St^+ correspond to those cases in which a continuously increasing $\mathscr{E}/\mathscr{A}$ ratio was observed during melting.

4. Summary and Conclusion

A thermal phase-field model constructed in the 'thin-interface' limit and incorporating a number of advanced numerical techniques such adaptive mesh refinement, implicit time-stepping and a multigrid solver has been used to study the isolated diffusive melting of elliptic dendritic fragments. The results of the simulations are found to be fully consistent with the experimental observation of such melting by [1, 2, 3] in that during most of the melting period the ratio of the semi-major to semi-minor axes, $\mathscr{E}/\mathscr{A}$, increases slowly with time, but that in the terminal stages of melting this ratio collapse rapidly to 1 as the fragment spheroidises just prior to extinction. The model confirms the assumption in [3] that, notwithstanding the change in $\mathscr{E}/\mathscr{A}$, the dendritic fragment retains, to a very good approximation, its elliptic cross-section throughout melting, with deviations from this only at the very tip of the fragment. The rate of melting is found not to be sensitive to the assumed value for the anisotropy of the surface energy, although the shape of the tip and its local curvature is a function of anisotropy.

One effect that could not be investigated experimentally is the effect of the melting Stefan number, St^+, on the evolution of the dendritic fragment. Here we find that the rate at which $\mathscr{E}/\mathscr{A}$ increases, and the maximum value that it attains, are sensitive functions of St^+, with high Stefan number favouring a greater increase in $\mathscr{E}/\mathscr{A}$. As experimentally both spatial and temporal variations in St^+ would have been likely during melting this may help explain why both melting at (approximately) constant $\mathscr{E}/\mathscr{A}$ and melting at slowly increasing $\mathscr{E}/\mathscr{A}$ were observed.

Unfortunately, while the current model may give some level of physical insight into the processes occurring during melting, direct comparison with experiment is not

currently possible. This is mainly due to the fact that the current simulations are 2-dimensional while it is well known that diffusively controlled processes are quantitatively different in 3-dimensions. Moreover, limitations in the experimental apparatus, which was designed to provide an isothermal environment upon cooling, not upon heating, mean that constant melting Stefan number was not maintained through out the heating cycle. Near a maximum heating rate an approximately constant Stefan number of 0.055 was achieved [3], although undertaking a 3-dimensional phase-field simulation for the melting of such a fragment (Ref. [3] reports one such with $\mathscr{C}$ = 7.5 mm and a total melting time of 40 s) would represent a massive computational challenge. The feasibility of making such a quantitative comparison is currently being evaluated using a newly developed 3-dimensional and massively parallel version [21] of the code reported here. However, the current model provides a useful adjunct to that in [], providing confirmation of one of the underlying assumptions in that model (constant $\mathscr{C}/\mathscr{S}$ for the majority of the melting), while also confirming theoretically the collapse of $\mathscr{C}/\mathscr{S}$ to 1 in the terminal stages of melting.

References

1. M.E. Glicksman, A. Lupulescu and M.B. Koss: J. Thermophys. Heat Tr., 2003, vol. 17, p. 69.
2. A. Lupulescu, M.E. Glicksman, and M.B. Koss: J. Cryst. Growth, 2005, vol. 276, p. 549.
3. M.E. Glicksman: Proc. of the 4th International Symposium on Physical Sciences in Space, Bonn-Bad Godesburg, Germany, July 2011. J. Phys. Conf. Ser. 327, 012001.
4. M.E. Glicksman, M.B. Koss, L.T. Bushnell, J.C. LaCombe, and E.A. Winsa: Adv. in Space Res., 1995, vol. 16, p. 181.
5. M.B. Koss, J.C. LaCombe, L.A. Tennenhouse, M.E. Glicksman, and E.A. Winsa: Metall. Mater. Trans. A, 1999, vol. 30A, p. 3177.
6. J.C. LaCombe, M.B. Koss, and M.E. Glicksman: Phys. Rev. Lett., 1999, vol. 83, p. 2997
7. Ivantsov GP. Doklady Akademii Nauk SSSR 1947; 58:567 (1947).
8. M.E. Glicksman, M.B. Koss, and E.A. Winsa: Phys. Rev. Lett., 1994, vol. 73, p. 573.
9. J.C. LaCombe, M.B. Koss, and M.E. Glicksman: Metall. Mater. Trans. A, 2007, vol. 38A, p. 116
10. A. Karma and W-J. Rappel: Phys. Rev. E, 1996, vol. 53, p. R3017.
11. A. Karma and W-J. Rappel: Phys. Rev. Lett., 1996, vol. 77, p. 4050.
12. J. Rosam, 'A fully implicit, fully adaptive multigrid method for multi-scale phase-field modelling', Ph.D. thesis, University of Leeds, 2007.
13. J. Rosam, P.K. Jimack and A.M. Mullis: J. Comp. Phys., 2007, vol. 225, p. 1271.
14. J. Rosam, P.K. Jimack and A.M. Mullis: Acta Mater., 2008, vol. 56, p. 4559.
15. A.M. Mullis: Comp. Mater. Sci., 2006, vol. 36, p, 345.
16. W. Hundsorfer & J.G. Verwer, Numerical Solution of Time-Dependant Advection-Diffusion-Reaction Equations, Springer-Verlag, 2003.
17. U. Trottenberg, C. Oosterlee and A. Schuller, Multigrid, Academic Press, 2001.
18. A. Brandt: Math. Comp., 1977, vol. 31, p. 333.
19. B. Echebarria, R. Folch, A. Karma, M. Plapp: Phys. Rev. E 2004, vol. 70 p. 061604.
20. S.P. Marsh & M.E. Glicksman: Acta Mater. 1996, vol. 44, p. 3761.

21. C. G. Goodyer, P. K. Jimack, A. M. Mullis, H. Dong, X. Yu: Adv. Appl. Math. Mech. 2012, vol. 4, p. 665.